

Spatial electron tunneling leads to space-charge-limited current in organic hole transport materials

Shaofeng Chen(陈绍枫), Yanfei Lu(鲁燕飞), Dongcheng Chen(陈东成), and Shi-Jian Su(苏仕健)
Citation: Chin. Phys. B, 2025, 34 (**7**): 078101. DOI: 10.1088/1674-1056/adcb1d
http://cpb.iphy.ac.cn; http://iopscience.iop.org/cpb

What follows is a list of articles you may be interested in

Extraordinary mechanical performance in charged carbyne

Yong-Zhe Guo(郭雍哲), Yong-Heng Wang(汪永珩), Kai Huang(黄凯), Hao Yin(尹颢), and En-Lai Gao(高恩来)
Chin. Phys. B, 2022, 31 (**12**): 128102. DOI: 10.1088/1674-1056/ac7bf8

Thin-film growth behavior of non-planar vanadium oxide phthalocyanine

Tian-Jiao Liu(刘天娇), Hua-Yan Xia(夏华艳), Biao Liu(刘标), Tim S Jones, Mei Fang(方梅), Jun-Liang Yang(阳军亮)
Chin. Phys. B, 2019, 28 (**8**): 088101. DOI: 10.1088/1674-1056/28/8/088101

Polarized red, green, and blue light emitting diodes fabricated with identical device configuration using rubbed PEDOT:PSS as alignment layer

Haoran Zhang(张皓然), Qi Zhang(张琪), Qian Zhang(张茜), Huizhi Sun(孙汇智), Gang Hai(海港), Jing Tong(仝静), Haowen Xu(徐浩文), Ruidong Xia(夏瑞东)
Chin. Phys. B, 2019, 28 (**7**): 078108. DOI: 10.1088/1674-1056/28/7/078108

Photodetectors based on small-molecule organic semiconductor crystals

Jing Pan(潘京), Wei Deng(邓巍), Xiuzhen Xu(徐秀真), Tianhao Jiang(姜天昊), Xiujuan Zhang(张秀娟), Jiansheng Jie(揭建胜)
Chin. Phys. B, 2019, 28 (**3**): 038102. DOI: 10.1088/1674-1056/28/3/038102

Progress in organic spintronics

Yang Fu-Jiang (杨福江), Han Shi-Xuan (韩士轩), Xie Shi-Jie (解士杰)
Chin. Phys. B, 2014, 23 (**5**): 058106. DOI: 10.1088/1674-1056/23/5/058106

Spatial electron tunneling leads to space-charge-limited current in organic hole transport materials

Shaofeng Chen(陈绍枫)[1,2,†], Yanfei Lu(鲁燕飞)[1,2,†], Dongcheng Chen(陈东成)[1,2,‡], and Shi-Jian Su(苏仕健)[1,2]

[1] *State Key Laboratory of Luminescent Materials and Devices, South China University of Technology, Guangzhou* 510640, *China*
[2] *Institute of Polymer Optoelectronic Materials and Devices, South China University of Technology, Guangzhou* 510640, *China*

(Received 14 January 2025; revised manuscript received 31 March 2025; accepted manuscript online 10 April 2025)

The injection of electrical charge from an electrode into organic semiconductors directly influences the performance of organic optoelectronic devices. However, our understanding of the mechanisms behind charge injection remains incomplete. In this study, we explored the hole injection from an indium tin oxide (ITO) electrode into a hole transport layer (HTL) by employing various organic interlayers (ILs) with different ionization potentials (IPs). It was demonstrated that using O_2 plasma treatment onto an ITO surface and incorporating an interlayer (IL) with a higher IP between the ITO electrode and the HTL can substantially increase the hole current density. This improvement leads to the achievement of barrier-free injection and the establishment of space-charge-limited current. We propose two synergistic mechanisms of spatial electron tunneling that govern the injection characteristics: electron tunneling from the HTL across the IL to the electrode that establishes an electrostatic equilibrium with a zero-injection barrier and an electric-field-induced spatial tunneling effect that occurs during device operation with applying bias. This research offers a strategy to achieve space-charge-limited hole current and provides an explanatory framework for understanding the underlying physics of charge injection.

Keywords: organic semiconductor, spatial electron tunneling, hole injection, indium tin oxide, work function

PACS: 42.70.Jk, 73.43.Jn, 81.05.Fb

DOI: 10.1088/1674-1056/adcb1d **CSTR:** 32038.14.CPB.adcb1d

1. Introduction

The interface is the device, as stated by Kroemer in 2000,[1] and later commented on in 2012.[2] This highlights the significance of understanding interface properties for optoelectronics. In contrast to its inorganic counterparts,[3–5] the issue of electrical injection has long been a fundamental concern in the field of organic semiconductor devices because of a lack of a heavily doping approach to generate Ohmic contacts at the electrode/semiconductor interface. An injection barrier universally exists at electrode/organic-semiconductor interfaces. The presence of this barrier typically leads to a reduction in carrier injection efficiency, resulting in low injection currents that eventually affect device efficiency. Besides, understanding the injection barrier at the interfaces is crucial for further elucidating optoelectronic device physics. For example, achieving ideal devices with sufficiently high injection current densities, which are crucial for applications like organic electrically pumped lasers and the high brightness of blue organic light-emitting devices, is impossible without overcoming the injection barrier. The characterization of electron and hole trapping in organic semiconductors also needs to carefully consider the influence of the injection barrier.[6–10] The injection barrier is closely connected with the interface properties at the electrode/organic semiconductor contact.

The hole injection barrier (ΔE_{I}) commonly defined as the energy difference between the work function (WF) of the electrode and the ionization potential (IP) of the organic hole transport layer (HTL)

$$\Delta E_{\mathrm{I}} = \mathrm{IP} - \mathrm{WF}. \tag{1}$$

The IP and WF are generally measured by ultraviolet photoelectron spectroscopy (UPS), then a ΔE_{I} value can be determined. It should be noted that the above definition of the injection barrier relies on the non-contact separated semiconductor materials, which does not reflect the actual injection barrier under electrical contact conditions in devices. Thus, for certain organic semiconductor devices, the clear correlation between the ΔE_{I} and injection current density may not be seen. Therefore, a definition of the effective injection barrier, denoted as $\Delta E_{\mathrm{I,e}}$, should be introduced to closely correlate the $\Delta E_{\mathrm{I,e}}$ with the injection current densities. For the vanishing of $\Delta E_{\mathrm{I,e}}$, the current density of materials without trapping should be space-charge-limited, according to the Mott–Gurney law.[11]

Indium tin oxide (ITO) is widely used as an anode in organic optoelectronics due to its superior optical and electrical properties, such as high transparency and conductivity,[12–16] as well as its compatibility with existing applications in industrial fields, including liquid crystal displays.[14] The published WF values of ITO with O_2 plasma treatment generally range

[†] These authors contributed equally to this work.
[‡] Corresponding author. E-mail: mschendc@scut.edu.cn

© 2025 Chinese Physical Society and IOP Publishing Ltd. All rights, including for text and data mining, AI training, and similar technologies, are reserved.

from 4.1 eV to 4.7 eV.[17–20] Tang *et al.* reported the value of 4.4–4.5 eV by using x-ray photoelectron spectroscopy (XPS) and UPS.[18] Our results for O_2 plasma ITO were 4.6 eV and 4.743 eV by using UPS and a Kelvin probe, respectively.[19] Nevertheless, the IP of organic HTLs commonly ranges from 5.0 eV to 5.8 eV, suggesting that the ΔE_I at an ITO/HTL interface normally covers the range 0.4–1.7 eV.

Several kinds of methods have been used to reduce the ΔE_I at an ITO/HTL interface. A straightforward approach is to enhance the effective WF of ITO, thus leading to a lower ΔE_I, such as electrode modification through chlorination and self-assembled layers to adjust the WF of electrodes within a wide range,[21–23] the use of metal oxides as hole injection layers,[24,25] and interfacial modification with strong electron acceptor materials.[26–28] Recent studies elucidating the energy-level alignment at the electrode–organic interface have significantly advanced our understanding of surface semiconductor properties.[29–32] Wetzelaer *et al.* proposed a strategy to add an organic interlayer with deeper ionization energy between the MoO_3 electrode modification layer and the organic transport layer to achieve Ohmic injection.[9] Although continuous efforts have been made to enhance the carrier injection from electrodes to organic semiconductors by interface engineering,[19,33–42] considerable challenges remain in understanding the injection mechanisms and achieving barrier-free injection. Questions to be explored include the carrier injection mechanisms at the electrode/semiconductor interface, connection between the ΔE_I and $\Delta E_{I,e}$, the proper energy landscape between the electrode, interlayer (IL) and HTL for hole injection, and the effect of the $\Delta E_{I,e}$ on the ideal current densities (theoretically maximum current density) of an organic semiconductor. Herein, hole injection from the ITO electrode to HTL was investigated by using various ILs with different IPs. We show that with the O_2 plasma treatment and addition of an IL with a higher IP between the ITO electrode and the HTL, the hole current density can be significantly enhanced, leading to barrier-free injection and space-charge-limited current (SCLC). We propose that the O_2 plasma treatment gives rise to the steep band bending at the ITO surface. Incorporating an IL with a higher IP between the ITO electrode and the HTL leads to energy level pinning at the IP of the HTL, thus resulting in a zero $\Delta E_{I,e}$. Two kinds of spatial electron tunneling, i.e., spatial electron tunneling from the HTL to the electrode to form electrostatic equilibrium conditions with a zero-injection barrier (relevant to energy landscape) and an electric-field-induced spatial tunneling effect under device operation, were analyzed to govern the injection performances. Eventually, we prove that an SCLC was indeed realized through the spatial electron tunneling effect by temperature-dependent current density–voltage analysis and simulation with a drift-diffusion model.

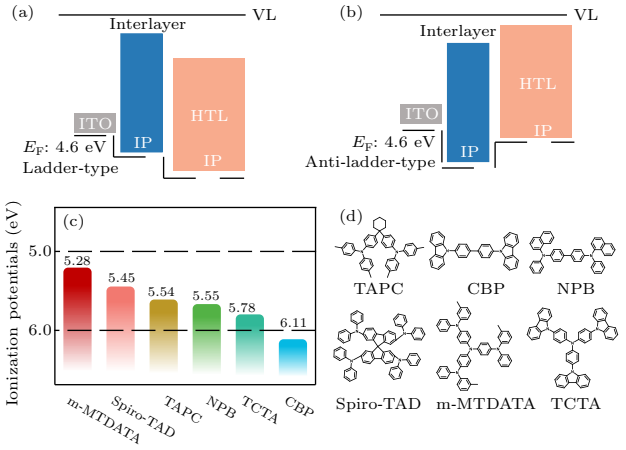


Fig. 1. Two different hole-injection strategies and the IP and molecular structures of the materials used. (a) Ladder injection: the IP of the IL is intermediate between the ITO and the HTL. (b) Anti-ladder-injection: the IP of the IL is deeper than the ITO and the HTL. (c) The IP of the IL and the HTL materials, which was obtained by atmospheric photoelectron spectroscopy AC-3. (d) The molecular structures of the materials used.

2. Results and discussion

Two kinds of energy landscapes (Figs. 1(a) and 1(b)) can be identified, which are denoted as ladder and anti-ladder types, according to the WF of the ITO electrode and the IPs of the IL and the HTL (Fig. 1(c)). To exclude the charge neutralization effect, we investigated the hole injection from an ITO electrode to an HTL by making hole-only devices. The typical device structure is ITO/IL/HTL/TCTA (5 nm)/MoO_3 (2.7 nm)/Al (100 nm). The layer configuration of TCTA/MoO_3/Al was used as a reference counter electrode to effectively hinder electron injection and provide the Ohmic contact for hole extraction.[9] 1,1-Bis[(di-4-tolylamino)phenyl]cyclohexane (TAPC) and N,N′-Di (1-naphthyl)-N,N′-diphenyl-(1,1′-biphenyl)-4,4′-diamine (NPB) were selected as the representative HTL. Several arylamine-based materials, including 4,4′,4″-Tris(N-3-methylphenyl-N-phenyl-amino)-triphenylamine (m-MTDATA), 2,2′,7,7′-Tetrakis(N,N-diphenylamino)-2,7-diamino-9,9-spirobifluorene (Spiro-TAD), NPB, 4,4′,4″-Tris(carbazol-9-yl)triphenylamine (TCTA), and 4,4′-Bis(carbazol-9-yl)biphenyl (CBP), were used as the ILs. All the molecular structures are shown in Fig. 1(d). It is worth mentioning that this is classified based on the non-contact energy levels of materials, which may not reveal the energy alignment in practical devices. For the ladder-type, the WF of electrode (ITO), IL and HTL increases sequentially; while for the anti-ladder-type device, the IL material has a deeper IP value than the electrode and HTL, which is different from the ladder-type device.

We first use the drift-diffusion model to investigate the current density–voltage characteristics for the ladder-type and anti-ladder-type devices. The device structure is designed as anode/IL1 or IL2 (5 nm)/HTL (180 nm)/cathode, where the IP or WF of anode, IL1, IL2, HTL and cathode are 5.0 eV,

5.28 eV, 5.78 eV, 5.54 eV, 5.0 eV, respectively. Other parameters used in the simulation can be found in Table S1. For the ladder-type injection device with IL1, the introduction of the IL significantly enhances the injection current densities. This is consistent with the experience in multilayer organic semiconductor devices, such as vacuum-evaporated organic light-emitting diodes.[43,44] In contrast, for the anti-ladder-type injection device, the introduction of the IL results in lower current densities, indicating that the IL acts as a barrier layer in this configuration.

We continue exploring the ladder-type and anti-ladder-type injections by fabricating devices. The series of hole-only device S1 with the structure of ITO (O_2 plasma)/X_1 (5 nm)/TAPC (180 nm)/TCTA (5 nm)/MoO_3 (2.7 nm)/Al (100 nm), where X_1 stands for no-IL, NPB, Spiro-TAD, TCTA and CBP, respectively, was fabricated to investigate the influence of different ILs. As shown in Figs. 2(a) and 2(c), the current density sequentially increases for the devices with Spiro-TAD, NPB, no-IL, and TCTA (1.73 mA/cm^2, 12.16 mA/cm^2, 36.10 mA/cm^2, 364.80 mA/cm^2, @2 V, respectively), while the devices with TCTA and CBP as the IL gives consistent current densities (364.80 mA/cm^2 versus 333.32 mA/cm^2). Comparing the current results with the IPs of the IL materials, we observe two key findings: (i) the ladder-type IL leads to reduced current injection, while the anti-ladder-type IL gives rise to significant enhancement of current density; (ii) the bigger IP offset between the IL and the HTL results in the lower current density for the ladder type; however, the IP offset hardly affects the injection current for the anti-ladder type. To further test the effectiveness of this method, we also investigated the devices employing NPB as the HTL and m-MTDATA and TCTA as the IL, which representatively acts as the ladder and anti-ladder cases (device series S2), as shown in the Figs. 2(b) and 2(d) . The NPB device utilizing TCTA as the IL exhibits a current density of 124.5 mA/m^2 at 2 V, which is two times larger than the reference device without IL (53.0 mA/cm^2 @2 V) and six orders of magnitude greater than the device with m-MTDATA (8.65×10^{-4} mA/cm^2 @2 V). This again proves the similar trend that devices with ILs forming the ladder-type energy landscape perform worse in terms of injection in contrast to the reference device without an IL, while for the anti-ladder scenario, a dramatic enhancement of current density can be obtained. To our surprise, these experimental results do not comply with the above-mentioned simulation based on the drift-diffusion model.

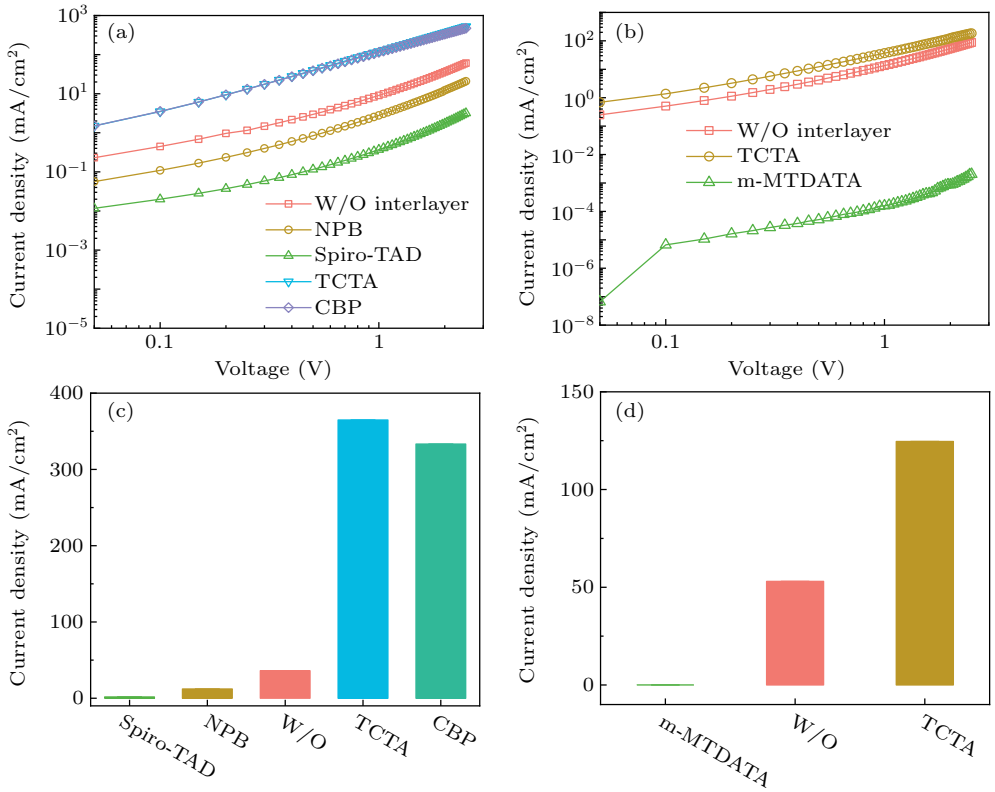


Fig. 2. Current densities of TAPC and NPB-based devices with O_2 plasma treatment on an ITO electrode incorporating different ILs. Current density–voltage characteristics of the devices: (a) ITO (O_2 plasma)/IL (no-IL, NPB, Spiro-TAD, TCTA, CBP, 5 nm)/TAPC (180 nm)/TCTA (5 nm)/MoO_3 (2.7 nm)/Al (120 nm); (b) ITO (O_2 plasma)/IL (no-IL, m-MTDATA, TCTA, 5 nm)/NPB (180 nm)/TCTA (5 nm)/MoO_3 (10 nm)/Al (120 nm). The current densities at 2 V with different situations of ILs: (c) TAPC-based devices; (d) NPB-based devices.

To explore the possible effect induced by the O_2 plasma treatment on ITO electrode, we further investigated the third series of devices S3 with the structure of ITO (no-plasma)/TCTA (w/ or w/o 5 nm)/TAPC (180 nm)/TCTA (5 nm)/MoO_3 (2.7 nm)/Al (100 nm). The current density–voltage characteristics are shown in Fig. 3(a). For ease of

comparison, the performances of their corresponding devices with O_2 plasma are also plotted in Fig. 3(a). To our surprise, the device with ITO (no-plasma)/TCTA (5 nm) shows dramatically reduced current density in contrast to that of the device with O_2 plasma treatment. Quantitatively, the current density of the former is 7.86×10^{-3} mA/cm^2 at 2 V, which is around five orders of magnitude less than that of the corresponding device with plasma (364.80 mA/cm^2 @2 V). Compared with the device without O_2 plasma treatment and an IL, the ITO (no-plasma)/TCTA (5 nm) device does not show obviously enhanced current density. Thus, it is clear that the O_2 plasma on ITO plays a key role in carrier injection.

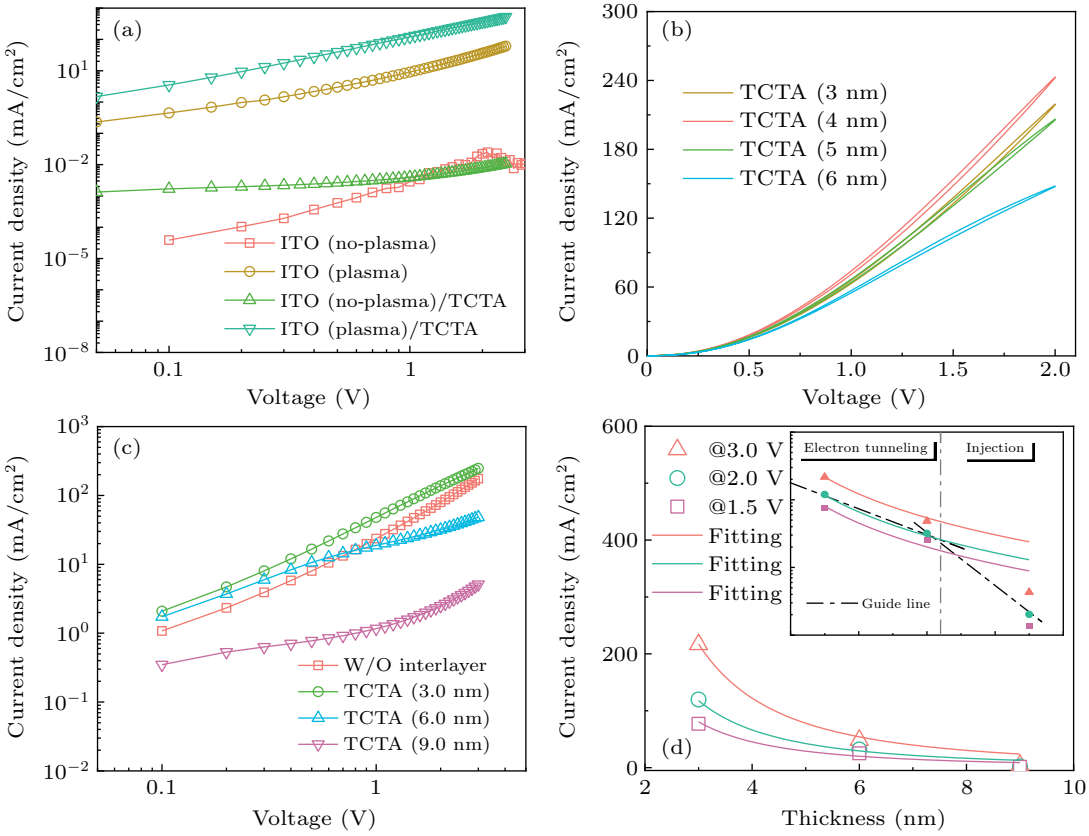


Fig. 3. The current density–voltage characteristics of devices fabricated with ITO substrates with and without plasma treatment and different interlayer thicknesses. (a) The comparative current density–voltage characteristics of the devices with the structure of ITO (w/ or w/o O_2 plasma)/TCTA (5 nm or none)/TAPC (180 nm)/TCTA (5 nm)/MoO_3 (2.7 nm)/Al (100 nm). (b) and (c) The current density–voltage characteristics of TAPC (180 nm) and NPB (200 nm) hole-only devices with different thickness IL TCTA, and TCTA (5 nm)/MoO_3 (10 nm)/Al (120 nm) as a cathode. (d) Fitting of thickness dependent current densities at different voltages by developing tunneling model of NPB (200 nm) hole-only devices. Inset: In log-coordination.

The thickness dependence of the IL was also investigated using the following device structure: ITO (O_2 plasma)/TCTA (3 nm, 4 nm, 5 nm, 6 nm)/TAPC (180 nm)/TCTA (5 nm)/MoO_3 (10 nm)/Al (120 nm) and ITO (O_2 plasma)/TCTA (none, 3.0 nm, 6.0 nm, 9.0 nm)/NPB (200 nm)/TCTA (5 nm)/MoO_3 (2.7 nm)/Al (100 nm). A strong dependence of the current densities on the IL thickness was observed (Figs. 3(b) and 3(c)). An optimized layer thickness for efficient current injection is about 5 nm. For devices with IL thickness exceeding that value, current densities decrease with increasing IL thickness. When the IL thickness reaches 9 nm, a significant injection barrier is introduced, resulting in lower current densities.

The metal-induced density of interface states model was first proposed by Flores and Tejedor *et al.*[45] Vázquez *et al.* applied this model to metal/organic interfaces, elucidating how weak chemical interactions between organic molecules and metals can generate significant induced density of interface states (IDIS).[46] To explore if the IDIS model can explain our observation, we made the following devices by using Au as the electrode: Au (40 nm)/TCTA (w or w/o 5 nm)/TAPC (180 nm)/TCTA (5 nm) /MoO_3 (10 nm)/Al (100 nm). It is interesting to find that the device employing Au (40 nm)/TCTA (5 nm) exhibits similar current densities to the corresponding device without a TCTA IL (Fig. S2). These results obtained using Au as the anode suggest that suppression of IDIS due to the metal-induced effect does not play a key role in devices with the same IL.

A literature investigation on the WF of ITO is shown in Table S3. The published WF values of ITO with O_2 plasma treatment generally range from 4.1 eV to 4.7 eV. We propose that the understanding of this experimental observation should be further developed. Before contact with organic semiconductors, the WF of ITO after O_2 plasma should be consid-

ered as two parts: the bulky region and the surface. Note that the WF is not strictly defined as a surface quantity in this work, since for nano systems with a thickness less than several nanometers, the concept of surface is blurred.[47] Furthermore, the surface behavior of ITO is difficult to measure precisely since the measurement process itself can alter its work function. As demonstrated in Fig. S3, a comparison is made between the current densities of devices fabricated using ITO substrates that have undergone AC-3 testing and those that did not. Notably, the WF of the tested samples exhibits significant variation compared to their untested counterparts. The WF of the bulky region is 4.6 eV, which matches well with the documented results. However, for the surface region, the WF descends abruptly, indicating the strong electron withdrawing capacity at the exact surface due to the O_2 plasma reaction. Since the fact that the common techniques like UPS do not separately reveal contributions from the bulk and surface regions, the surface induced by O_2 plasma should be extremely thin. Therefore, in the UPS test, the skin depth (Note S1) of ultraviolet light should penetrate into the bulk region of the ITO. So, the detected photoelectrons include contributions from both the bulk and the surface. This explanation gives the energy diagrams before contact for the ladder-type (Fig. 4(a)) and anti-ladder-type (Fig. 4(b)) systems, respectively. After contact between the electrode and organic semiconductors, the energy levels of the entire system realign due to the differing electron chemical potentials of the separated layers,[48] establishing a rebalanced electrostatic equilibrium. From the analysis of the non-contact case, the thickness of the surface interfacial layer induced by O_2 plasma should be extremely thin (approximately tens of atomic layers), thereby resulting in a low volumetric surface density of states. For the ladder-type system, since the IP of the IL is smaller than those of both the HTL and the band tail of ITO with O_2 plasma treatment, the valence electrons of the IL transfer to ITO surface states. Eventually, the energy levels at the ITO/IL interface are pinned at the IP of the IL (Fig. 4(c)) due to the low surface density of the O_2-plasma-induced states. Thus, an injection barrier (ΔE_{enl}) arises at the ITO/IL interface from the energy difference between adjacent layers in the ladder-type system. ΔE_{enl} depends functionally on the IP of the ILs in the ladder-type system because of the pinning effect. This fully explains the experimental results of ladder-type devices employing ILs with different IP values (e.g., Fig. 2(a), the case with NPB and Spiro-TAD).

We move on to discuss the energy alignment of anti-ladder-type system, which gives significantly enhanced current densities. A different re-aligned electrostatic equilibrium scheme, i.e., energy level alignment after contact, is developed. As shown in Fig. 4(d), electron transfer from the HTL to the band tail of ITO is considered to occur, since in the anti-ladder case the IP of the HTL is smaller than that of both the IL and the band tail of ITO with O_2 plasma treatment. This is a spatial tunneling effect from the HTL to the ITO electrode after fabrication of the devices. It gives the energy-level pinning at the IP of the IL, thus resulting in a zero value of ΔE_{enl}. Thus, if the IP of the IL is larger than IP of the HTL, the injection influence is the same. This is consistent with the experimental results in Fig. 2. Considering the results in the thickness-dependent experiment of the IL (Figs. 3(b) and 3(c)), we realized that after applying the forward bias to the device, there should be an electric-field-induced spatial tunneling effect that leads to electron transfer from the ITO electrode to the HTL. We developed a theoretical model to understand this process, and the details of the derivation are presented in Appendix A. Additionally, the fitted parameters and a detailed discussion are shown in Table S4. The current density dependence on IL thickness (Fig. 3(c)) can be well fitted by the developed tunneling model (Fig. 3(d)) for IL thicknesses below 6 nm. This indicates that the electron tunneling is responsible for the strong dependence of current densities on IL thickness.

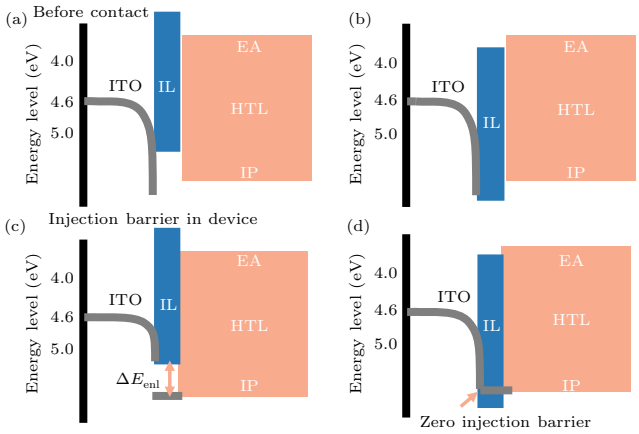


Fig. 4. The schematic energy-level diagram of the electrode/organic systems before contact: (a) ladder-type; (b) anti-ladder-type; and after contact in devices: (c) ladder-type with a significant injection barrier; (d) anti-ladder-type with zero injection barrier.

From the model, it is clear that if the thickness of the IL exceeds a critical value (approximately 6 nm), the injection current density is significantly decreased. The injection barrier introduced by the tunneling distance is denoted as ΔE_{tnl}. Therefore, the total $\Delta E_{\mathrm{I,e}}$ equals the sum of ΔE_{enl} and ΔE_{tnl}. This provides a comprehensive explanation for the current density–voltage characteristics of anti-ladder-type devices. We further emphasize that the root-mean-square (RMS) roughness of both ITO and TCTA (approximately 3 nm, as shown in Fig. S7) introduces topographical fluctuations, causing the actual thickness of vapor-deposited device layers to deviate from the electron tunneling distance. As illustrated in Fig. 3(b), the current density exhibits an initial increase followed by a decrease as the IL thickness increases. Specifically, when the IL is relatively thin, partial direct contact persists be-

tween the ITO and the HTL, resulting in a partial tunneling effect. When the IL thickness reaches a sufficient value to completely isolate ITO and HTL (with the minimum IL thickness acting as the threshold), the tunneling current attains its maximum. This rationale underpins the fitting process starting from 3 nm in Fig. 3(d). As the thickness further increases, the tunneling probability decreases sharply due to the increased barrier width. This mechanism is corroborated by the consistency between the optimal IL thickness (approximately 6 nm) and the RMS roughness (approximately 3 nm). Beyond this critical thickness, charge transport transitions from electron tunneling to a two-step process: injection from the electrode into the IL, followed by transport through the IL to the HTL. Since IL materials typically exhibit deep IP, electrode-to-IL injection becomes significantly impeded. This explains the sharp current density decline at greater thicknesses (e.g., 9 nm), which deviates from predictions based solely on electron tunneling models.

It is interesting that the most efficient hole injection in our representative model should require two kinds of spatial electron tunneling, i.e., spatial electron tunneling from the HTL to electrode to form electrostatic equilibrium conditions with zero ΔE_{enl}, and electric-field-induced spatial tunneling effect under device operation. The maximum injection single-carrier current is space-charge-limited. To explore if the anti-ladder strategy by spatial electron tunneling can lead to SCLC, we further made the following devices with the structure of ITO (O_2 plasma)/X_3/TAPC (180 nm)/TCTA (5 nm)/MoO_3 (10 nm)/Al (100 nm), where X_3 represents TCTA (5 nm), CBP (5 nm), MoO_3 (2.7 nm)/TCTA (5 nm), MoO_3 (2.7 nm)/CBP (5 nm), respectively. The devices containing MoO_3 were fabricated as the control devices. As shown in Fig. 5(a), all the devices with different ILs exhibit nearly the same current densities. It is interesting that the devices with and without MoO_3 have similar injection current densities. This suggests that the current is limited by bulky transport. The results show that a suitable IL can achieve a role comparable to the traditional MoO_3 electrode modification layer.

All these phenomena indicate that the current injection based on the spatial electron tunneling effect has reached its limit, suggesting the current may be governed by SCLC. According to the Mott–Gurney square law, the trap-free SCLC can be expressed as

$$J = \frac{9}{8}\varepsilon\mu\frac{V^2}{L^3}, \tag{2}$$

where ε is the dielectric constant, μ is the charge mobility, and L is the thickness of organic thin film. Under SCLC, the slope of the current density–voltage curve in a log–log diagram should be equal to 2. To eliminate the influence of built-in potential on the analysis, NPB, which exhibits symmetric forward and reverse current densities, was selected. Consequently, the slope of current density–voltage temperature-dependent of the IL was analyzed using the following device structure: ITO (O_2 plasma)/TCTA (5 nm)/NPB (160 nm)/TCTA (5 nm)/MoO_3 (10 nm)/Al (100 nm). The slope approximates 1.7 across temperature, as shown in the Fig. 5(b). Electrostatic energy-level alignment calculations predict carrier accumulation near the electrode/IL or IL/HTL interfaces (Fig. S4). Furthermore, drift-diffusion simulations only fit experimental results when doping is included (Fig. S6), indicating doping-like behavior in the current density. This carrier accumulation reduces the slope below 2. All these results imply that SCLC is achieved through the spatial electron tunneling.

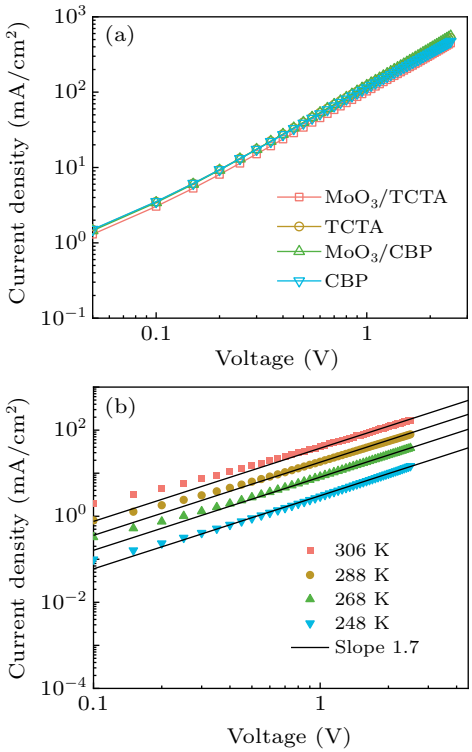


Fig. 5. (a) Current density–voltage characteristics of devices with the structure of ITO (O_2 plasma)/X_3/TAPC (180 nm)/TCTA (5 nm)/ MoO_3 (10 nm)/Al (100 nm), where X_3 represents TCTA (5 nm), CBP (5 nm), MoO_3 (2.7 nm)/TCTA (5 nm), MoO_3 (2.7 nm)/CBP (5 nm), respectively. (b) The slope of current density–voltage characteristics of the hole-only device at different temperatures for the structure ITO (O_2 plasma)/TCTA (5 nm)/NPB (160 nm)/TCTA (5 nm)/MoO_3 (10 nm)/Al (100 nm).

3. Conclusion

In summary, we investigated the current injection characteristics of hole-only devices employing an ITO/IL/HTL layer configuration, classified as ladder-type or anti-ladder-type based on the IPs of the constituent layers. For the anti-ladder case, the IP of the IL exceeds the bulk WF of both ITO and HTL. We found that the ladder-type ILs reduce current injection, while the anti-ladder-type ILs significantly enhance current density. A larger IP offset between the IL and HTL further decreases current density in ladder-type devices,

while the IP offset minimally affects injection currents in anti-ladder-type systems. We demonstrate that the $\Delta E_{\mathrm{I,e}}$ originates from two components: $\Delta E_{\mathrm{I,enl}}$ and $\Delta E_{\mathrm{I,tnl}}$. Our results confirm that introducing an anti-ladder-type high-IP IL with optimized thickness effectively reduces the energy barrier $\Delta E_{\mathrm{I,e}}$. An explanatory framework including two kinds of spatial electron tunneling, i.e., spatial electron tunneling from the HTL to the electrode to form electrostatic equilibrium conditions with zero ΔE_{enl} and electric-field-induced spatial tunneling effect under device operation, was used to interpret the experimental results. This work provides a straightforward and effective method to achieve hole injection approaching the SCLC regime while elucidating fundamental charge injection physics at electrode/organic semiconductor interfaces.

Appendix A

A1. Device fabrication and testing methods

All devices were fabricated on glass substrates precoated with a 95-nm-thick layer of ITO with a sheet resistance of 30 $\Omega\cdot\mathrm{sq}^{-1}$. The substrates were cleaned in sequence in ultrasonic bath of acetone, detergent, deionized water, isopropyl alcohol, and then treated by O_2 plasma for 2 min before device fabrication. The evaporation rates of the IL and the HTL are controlled by 0.1 $\text{Å}\cdot\mathrm{s}^{-1}$ and 1.0 $\text{Å}\cdot\mathrm{s}^{-1}$, respectively. All evaporations are done at a pressure lower than 3×10^{-4} Pa. The current density–voltage characteristics of all devices were assessed in a glovebox atmosphere, where the concentrations of oxygen and water were maintained below 0.1 ppm, utilizing a Keithley 2400 source meter for precise measurement. To obtain current density–voltage characteristic curves at various temperatures, nitrogen gas at room temperature was cooled by flowing through a copper tube connected to a tank filled with liquid nitrogen. The cooled nitrogen was then directed into the test chamber containing the devices under investigation. During measurements, a high-precision barometer monitored the gas path pressure, while a thermocouple measured the substrate temperature. The nitrogen flow rate was adjusted to maintain the substrate temperature within ±1 °C of the desired range.

A2. Simulation and numerical computation

For the simulation method, the equations of one-dimensional drift-diffusion model are discretized and solved by a home-made program using iteration method. Detailed calculations can be referenced in Refs. [49,50]. The electrostatic energy level alignment was determined by solving the Poisson equation without applying a bias, with the calculation expressions detailed in Note S2. The process for solving this was analogous to that of the one-dimensional drift-diffusion model. The global fitting of the tunneling current was implemented using Python programming, specifically by invoking the built-in minimize function to minimize a custom loss function that computes the overall error across all groups.

A3. Electron tunneling theory

The current density expression can be derived as follows:

$$J=\rho v=epv, \tag{A1}$$

where ρ is carrier density, v is the velocity of carriers, p is carrier concentration, p_0 is the carrier concentration. For organic semiconductors, the carrier primarily undergoes drift motion after injection, thus the carrier movement speed can be characterized by the bulk mobility of the material

$$J=ep\mu E, \tag{A2}$$

where μ represents the carrier mobility, and E is the electric field. In the presence of the interlayer, the carrier injected into the organic semiconductor is equivalent to the product of the carrier concentration p_0 from the electrode and the tunneling probability T

$$J=ep_0T\mu E. \tag{A3}$$

Consider the interlayer as a one-dimensional rectangular barrier, and for carriers of electrode, there is generally a situation where $E_k<V_0$, then we can get[51]

$$T=\frac{4k^2\beta^2}{(k^2+\beta^2)^2(\mathrm{sh}(\beta d))^2+4k^2\beta^2}, \tag{A4}$$

where $k=\sqrt{2m^*E_k/\hbar^2}$, $\beta=\sqrt{2m^*(V_0-E_k)/\hbar^2}$, and $\mathrm{sh}(\beta d)$ is a symbolic representation for a specific function

$$\mathrm{sh}(\beta d)=\frac{\mathrm{e}^{\beta d}-\mathrm{e}^{-\beta d}}{2}. \tag{A5}$$

Here, m^* represents the effective mass of the carrier, $\hbar$ is the reduced Planck constant, E_k is the kinetic energy of the carrier before penetrating the barrier, V_0 is the height of the barrier, and d is the width of the barrier. E_k can be further expressed as

$$E_k=\frac{1}{2}m^*v^2. \tag{A6}$$

Generally, after tunneling, the kinetic energy of the carrier remains nearly unchanged, so the velocity of the carrier can also be represented by the bulk mobility of the material. Therefore, we have

$$E_k=\frac{1}{2}m^*(\mu E)^2. \tag{A7}$$

Finally, we obtain an expression for the device current density in the scenario where an interlayer is present

$$J=ep_0\frac{4k^2\beta^2}{\left(k^2+\beta^2\right)^2(\mathrm{sh}(\beta d))^2+4k^2\beta^2}\mu E. \tag{A8}$$

Acknowledgments

Project supported by the National Key Research and Development Program of China (Grant No. 2020YFB0408000), Guangdong Provincial Department of Science and Technology (Grant No. 2019TQ05C778), and Guangdong Basic and Applied Basic Research Foundation (Grant No. 2019A1515011639).

References

[1] Kroemer H 2000 *Nobel Prize lecture*
[2] 2012 *Nat. Mater.* **11** 91
[3] Zheng Y, Gao J, Han C and Chen W 2021 *Cell. Rep. Phys. Sci.* **2** 100298
[4] Zhang X J, Shao Z B, Zhang X H, He Y Y and Jie J S 2016 *Adv. Mater.* **28** 10409
[5] Tung R T 2014 *Appl. Phys. Rev.* **1** 011304
[6] Sachnik O, Tan X, Dou D, Haese C, Kinaret N, Lin K H, Andrienko D, Baumgarten M, Graf R, Wetzelaer G J A H, Michels J J and Blom P W M 2023 *Nat. Mater.* **22** 1114
[7] Khodabakhshi E, Klockner B, Zentel R, Michels J J and Blom P W M 2019 *Mater. Horiz.* **6** 2024
[8] Abbaszadeh D, Kunz A, Wetzelaer G A H, Michels J J, Craciun N I, Koynov K, Lieberwirth I and Blom P W M 2016 *Nat. Mater.* **15** 628
[9] Kotadiya N B, Lu H, Mondal A, Ie Y, Andrienko D, Blom P W M and Wetzelaer G J A H 2018 *Nat. Mater.* **17** 329
[10] Kotadiya N B, Mondal A, Blom P W M, Andrienko D and Wetzelaer G J A H 2019 *Nat. Mater.* **18** 1182
[11] Mott N F and Gurney R W 1940 *Electronic Processes in Ionic Crystals* (Oxford: Oxford University Press)
[12] Ellmer K 2012 *Nat. Photonics* **6** 808
[13] Ren Y, Zhao G Y and Chen Y Q 2011 *Appl. Surf. Sci.* **258** 914
[14] Hecht D S, Hu L B and Irvin G 2011 *Adv. Mater.* **23** 1482
[15] Chen L J, Niu G X, Niu L B and Song Q L 2022 *Chin. Phys. B* **31** 038802
[16] Liu J M and Zhang D L 2023 *Chin. Phys. B* **32** 064208
[17] Parker I D 1994 *J. Appl. Phys.* **75** 1656
[18] Park Y, Choong V, Gao Y, Hsieh B R and Tang C W 1996 *Appl. Phys. Lett.* **68** 2699
[19] Chen D C, Zhou H, Cai P, Sun S, Ye H, Su S J and Cao Y 2014 *Appl. Phys. Lett.* **104** 053304
[20] Nehate S D, Prakash A, Mani P D and Sundaram K B 2018 *ECS Journal of Solid State Science and Technology* **7** P87
[21] Helander M G, Wang Z B, Qiu J, Greiner M T, Puzzo D P, Liu Z W and Lu Z H 2011 *Science* **332** 944
[22] Deng J, Hu D, Zhang Z, Zong B, Meng X, Sun Q, Shen B, Kang B and Silva S R P 2022 *J. Alloys Compd.* **911** 164983
[23] Huang F, Liu H, Li X and Wang S 2022 *Chem. Eng. J.* **427** 131356
[24] Shizuo T, Koji N and Yasunori T 1996 *J. Phys. D: Appl. Phys.* **29** 2750
[25] Greiner M T, Helander M G, Tang W M, Wang Z B, Qiu J and Lu Z H 2011 *Nat. Mater.* **11** 76
[26] Zhou X, Blochwitz J, Pfeiffer M, Nollau A, Fritz T and Leo K 2001 *Adv. Funct. Mater.* **11** 310
[27] Koch N, Duhm S, Rabe J P, Vollmer A and Johnson R L 2005 *Phys. Rev. Lett.* **95** 237601
[28] Park S M, Kim Y H, Yi Y, Oh H Y and Won Kim J 2010 *Appl. Phys. Lett.* **97** 063308
[29] Wang Q, Yang J, Gerlach A, Schreiber F and Duhm S 2022 *J. Phys.: Mater.* **5** 044010
[30] Duhm S 2022 *Electronic Structure* **4** 034003
[31] Koch N 2021 *Appl. Phys. Lett.* **119** 260501
[32] Zojer E, Taucher T C and Hofmann O T 2019 *Adv. Mater. Interfaces* **6** 1900581
[33] Chen D, Zhang C, Zhou H, Li X, Wang Z, Su S and Cao Y 2015 *ACS Appl. Mater. Inter.* **7** 3133
[34] Chen D C, Zhou H, Li X C, Liu M, Ye H, Su S J and Cao Y 2014 *Org. Electron.* **15** 1197
[35] Chen D C, Zhou H, Liu M, Zhao W M, Su S J and Cao Y 2013 *Macromol. Rapid. Comm.* **34** 595
[36] He Z C, Zhong C M, Su S J, Xu M, Wu H B and Cao Y 2012 *Nat. Photonics* **6** 591
[37] Liu S J, Zhang Z P, Chen D C, Duan C H, Lu J M, Zhang J, Huang F, Su S J, Chen J W and Cao Y 2013 *Sci. China Chem.* **56** 1119
[38] Zhou Y H, Fuentes-Hernandez C, Shim J, Meyer J, Giordano A J, Li H, Winget P, Papadopoulos T, Cheun H, Kim J, Fenoll M, Dindar A, Haske W, Najafabadi E, Khan T M, Sojoudi H, Barlow S, Graham S, Brédas J L, Marder S R, Kahn A and Kippelen B 2012 *Science* **336** 327
[39] Lin J, Dai X L, Liang X Y, Chen D S, Zheng X R, Li Y F, Deng Y Z, Du H, Ye Y X, Chen D, Lin C, Ma L Y, Bao Q Y, Zhang H B, Wang L J, Peng X G and Jin Y Z 2020 *Adv. Funct. Mater.* **30** 1907265
[40] Wang C F, Li W D, Zeng Q, Liu X J, Fahlman M and Bao Q Y 2023 *Chin. J. Chem.* **41** 3792
[41] Fahlman M, Fabiano S, Gueskine V, Simon D, Berggren M and Crispin X 2019 *Nat. Rev. Mater.* **4** 627
[42] Peng X, Hu L, Qin F, Zhou Y H and Chu P K 2018 *Adv. Mater. Interfaces* **5** 1701404
[43] Kuwabara Y, Ogawa H, Inada H, Noma N and Shirota Y 1994 *Adv. Mater.* **6** 677
[44] Ho S H, Liu S Y, Chen Y and So F 2015 *J. Photon. Energy* **5** 057611
[45] Flores F and Tejedor C 1987 *J. Phys. C: Solid State Phys.* **20** 145
[46] Vázquez H, Oszwaldowski R, Pou P, Ortega J, Pérez R, Flores F and Kahn A 2004 *Europhys. Lett.* **65** 802
[47] Kahn A 2016 *Materials Horizons* **3** 7
[48] Wurfel P 1982 *J. Phys. C: Solid State Phys.* **15** 3967
[49] Koster L J A, Smits E C P, Mihailetchi V D and Blom P W M 2005 *Phys Rev B* **72** 085205
[50] Röhr J A, Moia D, Haque S A, Kirchartz T and Nelson J 2018 *J. Phys.: Condens. Matter* **30** 105901
[51] Griffiths D J and Schroeter D F 2018 *Introduction to quantum mechanics* (3rd Edn.) (Cambridge: Cambridge University Press)